PHOTONICS Research

Achieving full grating-lobe-free field of view with low-complexity co-prime photonic beamforming transceivers

Aroutin Khachaturian,* Reza Fatemi, and Ali Hajimiri

California Institute of Technology, Pasadena, California 91125, USA
**Corresponding author: akhachat@caltech.edu*

Received 29 July 2021; revised 9 March 2022; accepted 24 March 2022; posted 25 March 2022 (Doc. ID 437518); published 29 April 2022

Integrated photonic active beamforming can significantly reduce the size and cost of coherent imagers for LiDAR and medical imaging applications. In current architectures, the complexity of photonic and electronic circuitry linearly increases with the desired imaging resolution. We propose a novel photonic transceiver architecture based on co-prime sampling techniques that breaks this trade-off and achieves the full (radiating-element-limited) field of view (FOV) for a 2D aperture with a single-frequency laser. Using only order-of-N radiating elements, this architecture achieves beamwidth and sidelobe level (SLL) performance equivalent to a transceiver with order-of-N^2 elements with half-wavelength spacing. Furthermore, we incorporate a pulse amplitude modulation (PAM) row–column drive methodology to reduce the number of required electrical drivers for this architecture from order of N to order of $\sqrt{N}$. A silicon photonics implementation of this architecture using two 64-element apertures, one for transmitting and one for receiving, requires only 34 PAM electrical drivers and achieves a transceiver SLL of −11.3 dB with 1026 total resolvable spots, and 0.6° beamwidth within a 23° × 16.3° FOV.

https://doi.org/10.1364/PRJ.437518

1. INTRODUCTION

Solid-state photonic platforms provide an integration pathway for many photonics applications ranging from communications and medical imaging [1] to inertia sensors [2] and LiDAR imagers [3–5]. In particular, integrated active beamformers, also known as optical phased arrays (OPAs), implemented in silicon photonic platforms have the potential to perform complex and high-speed wavefront manipulation and processing on a single mass-producible chip [4,6–8], and can outperform their bulk optics and microelectromechanical systems (MEMS) counterparts [9,10]. This can lead to lens-free, miniaturized, and low-cost coherent imaging systems with applications in LiDAR scanners, robotics, bio-medical imaging, optical communication, and remote sensing. Early efforts in the past decade have focused on demonstrating different architectures for chip-scale photonic beamforming systems [8,11–13]. In these systems, implementation complexity significantly increases from the photonic front-end for wavefront manipulation and processing to the back-end for electrical processing as the number of resolvable spots scales. As the number of pixels increases, the required number of photonic radiators, phase shifters, and electrical interconnect nodes grows, and the overall power consumption, form factor, and cost can become prohibitive. For instance, to address the interconnect density challenge, complex and costly electrical interconnect solutions such as through-silicon via (TSV) [14], monolithic platforms [11], or large-scale chip-to-chip interposers are investigated [15]. Alternatively, full wavefront control can be sacrificed with architectures that can do only simple beamforming to reduce the interconnect density challenges [11,16,17].

These scalability bottlenecks are the direct result of OPA architectural choices. The most common solid-state 2D steerable beamformers primarily utilize OPAs with 1D apertures [6,7,11,17,18], as shown in Fig. 1(a). These OPAs rely on long wavelength-sensitive grating-based radiators in conjunction with a widely tunable integrated laser to steer the beam in one direction by around 20° [6,17,19] and steer in the perpendicular direction via phase tuning. These architectures require a rapidly tunable laser, and typically require rapid wavelength tuning over about 100 nm of wavelength (dictated by beam scanning rates), resulting in high-complexity and high-cost widely tunable laser sources. Furthermore, 1D OPAs cannot perform additional complex wavefront processing along the direction steered by the wavelength. Figure 1(b) shows the laser wavelength tuning range required to achieve the desired field of view (FOV) for several 1D OPA implementations. An important performance metric is the complexity order of the system, defined as the number of integrated components

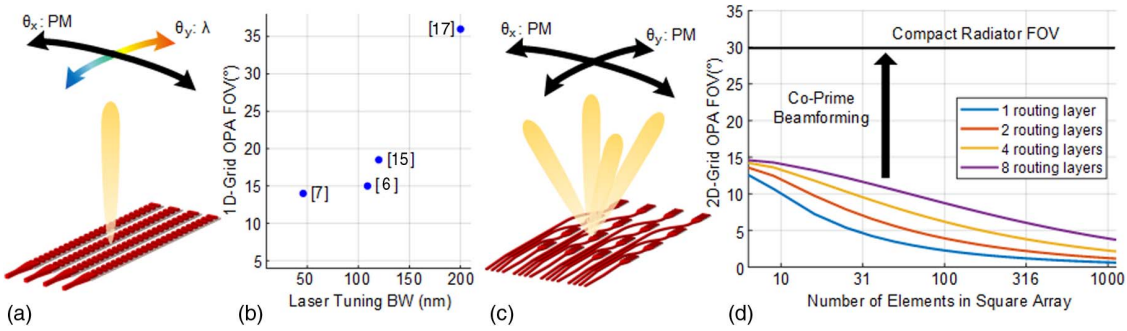

Fig. 1. Solid-state beam steering methods. (a) 1D-grid aperture beam steering with a tunable laser source. (b) FOV of 1D apertures as a function of wavelength tuning range for prior art [6,7,15,17]. (c) 2D-grid aperture beam steering with a fixed-wavelength laser. (d) FOV of 2D-grid uniform apertures as a function of the number elements in the array for a different number of photonics routing layers. 2D-grid co-prime transceiver OPAs can operate in a radiating-element-limited FOV regime using a single frequency source.

required compared to the number of resolvable spots. As a baseline, 1D OPAs, which require N phase shifters and N radiators for N resolvable spots, have a complexity of order N.

On the other hand, 2D apertures, as shown in Fig. 1(c), can operate with a low-cost single-wavelength laser. Moreover, 2D OPAs can, in principle, surpass the beam steering limitation imposed by a tunable laser's finite wavelength-sweep range, and fully phase-controlled 2D OPAs can generate arbitrary wavefronts; however, they require a 2D grid of radiators and corresponding phase shifters, and hence the system complexity is of the order of N^2. In addition to this increased system complexity, 2D apertures suffer from planar integrated photonic routing limitations, resulting in a limited effective FOV [4]. In this scenario, routing photonics waveguides to inner elements of the array requires a large pitch between the individual radiating elements. Furthermore, this pitch itself has to increase with an increasing number of elements, resulting in very poor scaling to large arrays. For planar photonics platforms with dielectric waveguides and radiators, this pitch is greater than half the wavelength. For arrays with larger than half-wavelength element spacing, the angular spacing of the grating lobes is calculated using

$$\theta_{\mathrm{GL}} = \arcsin(\lambda/d_x), \tag{1}$$

where d_x is the pitch of the radiating elements, and λ is the wavelength [20]. This effectively limits the useful FOV of the aperture to the angular spacing of two grating lobes in an array.

While multi-layer photonics platforms [21] may alleviate this problem to a limited degree, they do not come anywhere close to solving it. Figure 1(d) shows the trade-off between the number of radiators in an array and the effective grating-lobe-limited FOV for different numbers of photonic routing layers. For this plot, we assumed that the radiating elements are 2 μm × 2 μm, the waveguide width is 500 nm, and the minimum spacing between waveguides and radiators is 500 nm. The signal is routed from the four sides of the aperture to the inner elements of the array. Moreover, multi-layer processes increase this routing density. For example, a photonics process with two routing layers can route twice as many waveguides to the inner elements of the apertures. Afterwards, the minimum achievable pitch given these constraints is calculated for the different number of elements in the array, and Eq. (1) is used to calculate the FOV of the apertures. In this calculation, we assumed idealized loss-less bends and polarization-insensitive radiators. Furthermore, we assumed that 500 nm spacing would be sufficient to avoid electromagnetic coupling for very larger apertures. All of these assumptions result in Fig. 1(d) being an overestimation of apertures' FOVs that can be realized in practice. Nonetheless, the general trend in Fig. 1(d) holds. One approach to ameliorate the 2D OPA routing constraint is to design a non-uniform sparse array [22] that can suppress the grating lobes. The randomized positions of OPA radiating elements in a 2D grid can be optimized to achieve the desired beamwidth and sidelobe level (SLL), and meet planar photonics routing constraints. Alternatively, one can use other array beamforming techniques such as vernier arrays [23] to relax photonic routing limitations. However, the system complexity order of a 2D-grid aperture remains a challenge.

This work addresses the 2D-grid aperture OPA system complexity challenge using co-prime sampling techniques in uniform arrays with order-of-N system complexity instead of order-of-N^2 complexity. We demonstrate this approach using a novel transceiver OPA architecture with a 2D-grid aperture that resolves the 2D routing constraints and simplifies implementation complexity. This transceiver architecture results in an effective FOV primarily limited by the individual radiating element pattern. It operates with a single-wavelength laser while maintaining an order-of-N system complexity, similar to its 1D-grid OPA counterparts. This is achieved by co-designing the transmitter and receiver apertures with co-prime radiating element spacing, which leads to co-prime angular beam spacing that overlaps only in a single direction. Furthermore, we incorporate a row–column driver configuration that further reduces electronic drive circuitry complexity to the order of $\sqrt{N}$. We present the implementation of such a co-prime transceiver OPA in a standard silicon photonics process achieving a full (radiator-limited) FOV and 1026 resolvable spots. This 2D-grid co-prime transceiver architecture with two 8 × 8 transmitter and receiver apertures, a fixed-wavelength laser source, and 34 electrical pulse amplitude modulation (PAM) drivers, achieves angular resolution similar to a 32-element 1D-grid OPA with a tunable laser, or a 32 × 32-element 2D-grid OPA with a fixed-wavelength laser.

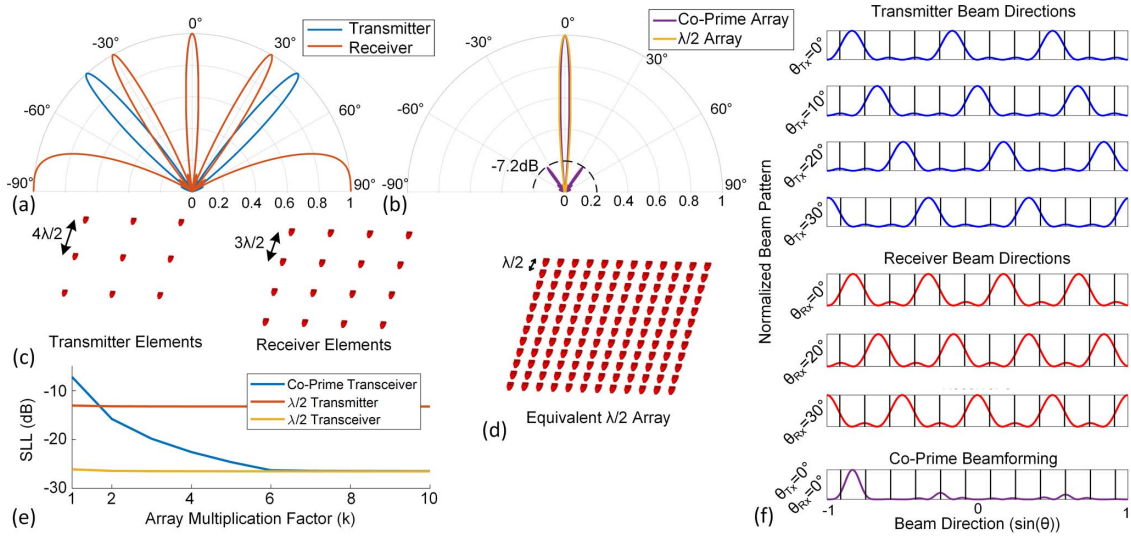

Fig. 2. Co-prime beamforming example for $P = 3$, $Q = 4$. (a) Cross section of the co-prime transmitter and receiver far-field radiation patterns. (b) Cross section of the transceiver co-prime beam showing no grating lobes and the equivalent half-wavelength spacing array far-field radiation pattern. (c) Co-prime transmitter and receiver array elements on larger than half-wavelength spacing grid. (d) Half-wavelength spacing array with beamwidth equivalent to the co-prime array. (e) Transceiver SLL as a function of array multiplication factor k. (f) Co-prime array beam steering for several directions and the resulting transceiver pattern for $\theta_{\mathrm{Rx}} = 0°$ and $\theta_{\mathrm{Tx}} = 0°$.

2. CO-PRIME OPTICAL BEAMFORMING

The presented photonic co-prime phased array utilizes co-prime sampling [24,25] to synthesize a transceiver pattern with no grating lobes (no aliasing) using 2D-grid transmitter and receiver OPAs with larger than half-wavelength spacing. A phased array transceiver with independent transmitter and receiver apertures, co-located in close proximity to each other, has an overall transceiver beam pattern given by the product of the transmitter and receiver array factors:

$$P_{\mathrm{TRx}}(\theta, \theta_{\mathrm{Rx}}, \theta_{\mathrm{Tx}}) = P_{\mathrm{Rx}}(\theta, \theta_{\mathrm{Rx}}) \cdot P_{\mathrm{Tx}}(\theta, \theta_{\mathrm{Tx}}) \cdot \rho(\theta), \quad \textbf{(2)}$$

where θ_{RX} and θ_{TX} are beam steering directions for the two arrays, and ρ is the reflection coefficient of the imaging target. If the transmitter and receiver element spacings (d_{TX} and d_{RX}) are defined to be co-prime integers within a constant factor of each other, $d_{\mathrm{TX}} = Pd_x$ and $d_{\mathrm{RX}} = Qd_x$, where P and Q are co-prime integers, the transmitter radiates in several directions, and the receiver receives from several directions; however, only one of those received directions overlaps with one of the transmitted directions. Furthermore, the transceiver array will have a synthesized pattern with grating lobes equivalent to two uniform transmitter and receiver arrays with d_x radiating element pitch. If $d_x = \lambda/2$, then the synthesized transceiver will have no grating lobes in the FOV. In other words, co-prime spacing of the transmitter and receiver elements suppresses the grating lobes and enables 2D beam steering over the full FOV limited by the radiation pattern of individual elements.

Figure 2 shows an example of co-prime beamforming using co-prime integers $P = 3$ and $Q = 4$. The transmitter array contains $N_{\mathrm{Tx}} = 4$ elements with $d_{\mathrm{Tx}} = 3\lambda/2$ spacing, and the receiver comprises $N_{\mathrm{Rx}} = 3$ elements with $d_{\mathrm{Rx}} = 4\lambda/2$. While the transmitter and receiver arrays contain three and four grating lobes, respectively [Fig. 2(a)], the synthesized transceiver pattern shown in Fig. 2(b) contains no grating lobes. The transmitter and receiver beams can be steered to resolve all the pixels within the FOV. Figure 2(f) shows several transmitter and receiver beam steering configurations. Combining any of the transmitter and receiver beams directions will have no grating lobes.

The number of transmitter and receiver elements can be increased to $N_{\mathrm{Tx}} = k_1 Q$ and $N_{\mathrm{Rx}} = k_2 P$ with $k_1, k_2 > 1$ to reduce SLL. Figure 2(e) shows the relationship between SLL and the common array size multiplication factor $k = k_1 = k_2$ for the array in Fig. 2(c). It is clear that $k = 2$ is sufficient for the co-prime transceiver OPA to surpass the SLL of uniform transmitter OPA, and $k = 6$ is sufficient for the co-prime transceiver OPA SLL to reach those of a half-wavelength spacing transceiver OPA.

The 2D-grid OPA in Fig. 2(c) with $k = 1$ has a beamwidth of 6.3° and can resolve 748 points. This transceiver contains $Q^2 = 16$ transmitter radiators and $P^2 = 9$ receiver radiators. A half-wavelength spacing transmitter OPA with the same number of spots, as shown in Fig. 2(d), will require $(PQ)^2 = 144$ radiators and phase shifters to achieve the same beamwidth as the co-prime variant [Fig. 2(b)]. For a factor N defined as $N = PQ$, co-prime OPAs with N elements achieve beamwidth performance similar to uniform N^2-element OPAs with half-wavelength element spacing. Hence, the system complexity is reduced from the order of N^2 to the order of N.

3. DESIGN

A silicon photonics co-prime transceiver was designed and implemented using the Advanced Micro Foundry's (AMF's) standard photonics foundry to demonstrate co-prime beamforming capability. Figure 3(a) shows the block diagram of the chip. Coupled power into the chip splits equally between the transmitter block for illumination beamforming and the

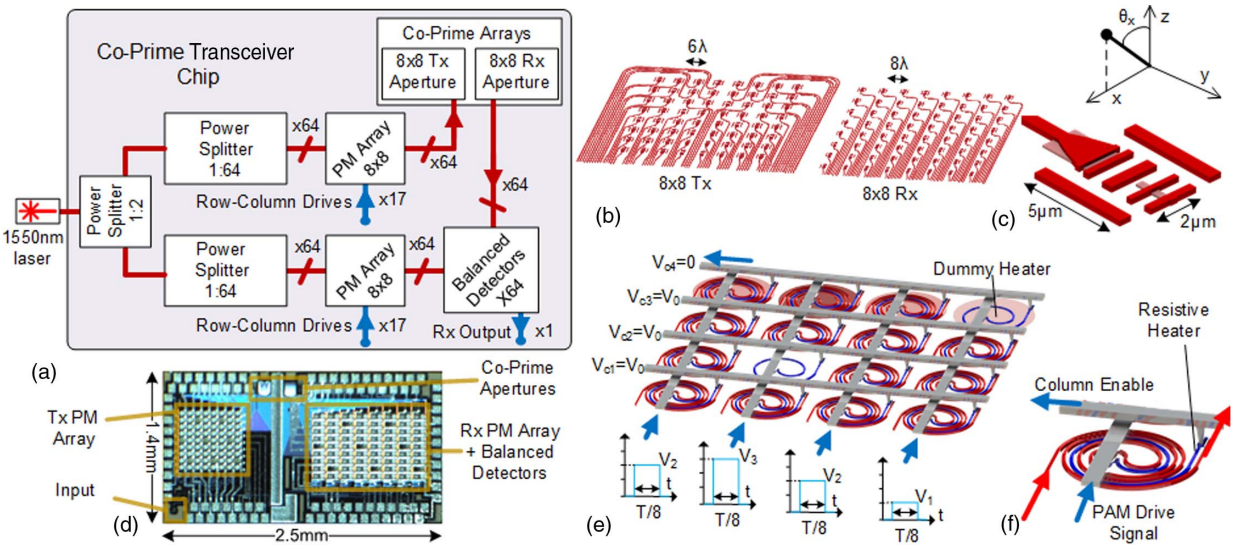

Fig. 3. Co-prime transceiver system architecture. (a) Block diagram of the co-prime transceiver. (b) Transmitter and receiver aperture implementations. (c) Compact radiator design. (d) Die photo of the fabricated chip. (e) Row–column drive phase modulator (PM) array. (f) Compact spiral thermal phase shifter.

receiver array for receiver beamforming and heterodyne detection [4]. An 8 × 8 array of transmitter elements and an 8 × 8 array of receiver elements [Fig. 3(b)] with equal power distribution are used. The equivalent uniform array pitch is $d_x = 2\lambda$, which results in a usable FOV of 30°. The co-prime numbers are $P = 3$ and $Q = 4$. This results in a transmitter array with $6\lambda = 9.2$ μm element pitch (grating lobes at 9.55°) and a receiver array with $8\lambda = 12.4$ μm element pitch (grating lobes at 7.18°) for an operational wavelength of 1550 nm. The proposed co-prime apertures with $P = 3$, $Q = 4$, and 8 × 8 elements require the array multiplication factors to be $k_1 = 2$ and $k_2 = 2.67$. This means the ideal SLL should be better than −15 dB with 0.65° beamwidth.

A compact 2 μm × 5 μm radiating element was optimized and implemented as the transmitting and receiving element [Fig. 3(c)]. This compact radiator has a 3 dB far-field beamwidth of 23° × 16.3°, which becomes the FOV-limiting factor in this design. The 1 dB spectral bandwidth of the radiator is over 400 nm, making the radiators very robust to changes in the operating wavelength. At the operating wavelength of 1550 nm, the peak radiation efficiency is at $\theta_y = 7.4°$.

Both transmitter and receiver OPAs contain an 8 × 8 array of phase modulators for complete relative phase control between radiator elements in each block. A cascade of Y-junctions divides the power equally among 64 radiating elements. A compact spiral thermo-optic phase shifter is designed for improved modulation efficiency and reduced cross talk as shown in Fig. 3(f). This spiral thermo-optic phase shifter has been previously characterized in Ref. [22] with 21.2 mW required electrical power for 2π phase shift and 19 kHz electro-optic modulation bandwidth. In addition, a series of dummy thermal heaters is distributed across the thermo-optic phase shifters to compensate for the temperature gradients on-chip. The phase shifters are connected in a row–column grid [Fig. 3(e)], resulting in a total of 34 electrical connections.

These row and column nodes are driven in a row–column fashion using time-domain demultiplexing [22]. Phase shifters are programmed one column at a time using switching electrical drivers. Seventeen PAM drivers continuously program the thermo-optic phase shifters where each column is active for 1/8 of the cycle T and receives eight times the required power. Therefore, the switching electrical drivers have a $\sqrt{8}$ increased drive voltage requirement. Given the kilohertz-range bandwidth of the modulators, cycling through the columns at megahertz frequencies ($T = 4$ MHz) ensures that the phase shifters receive constant electrical power. This row–column modulation reduces system interconnect and drive complexity by allowing $2N + 1$ drivers (+1 for the additional dummy heaters) to control N^2 thermo-optic phase shifters independently at the cost of requiring electrical drivers with increased bandwidth and drive voltage requirements. Independent control of the phase shifters allows for calibration of random relative phase errors between different phase shifters due to fabrication nonidealities, which is more significant for larger systems. Such high-speed and high-drive-voltage electrical drivers have been previously demonstrated using CMOS electronics [22]. Therefore, PAM row–column drivers can reduce the interconnect complexity from order N to order $\sqrt{N}$ without sacrificing complex beamforming capability.

The receiver array is configured as a heterodyne receiver with local oscillator (LO) path phase-shifting for improved receiver signal-to-noise ratio (SNR) [4]. The electrical output of all balanced detectors is combined on-chip to benefit from the array gain factor and boost SNR in the output signal prior to off-chip amplification and detection. The entire design is 2.5 mm × 1.4 mm as shown in Fig. 3(d).

4. MEASUREMENTS

A photonic far-field pattern measurement setup was constructed for the transceiver. The setup has a far-field transceiver

probe that can move along the hemisphere (θ_x and θ_y) with the co-prime OPA transceiver chip placed at the center of the hemisphere as shown in Fig. 4. The transceiver probe always points toward the center of the sphere at a constant 5 cm distance. This probe is constructed by placing a cleaved-fiber adjacent to an InGaAs photodetector die as shown in Fig. 4. The center-to-center distance of the photodiode's active area and the fiber core is less than 250 μm. However, the ideal transmitter and receiver beamwidth (0.6°) results in a 520 μm spot size, which is larger than the transceiver probe. As a result, in all transmitter and receiver measurements, the transmitter and receiver main beams overlap. This setup has an external lithium niobate ($LiNbO_3$) amplitude modulator (AM) for transmitter measurement followed by a pair of external single-sideband (SSB) $LiNbO_3$ modulators for receiver characterization. Furthermore, this setup allows for independent transmitter and receiver characterization with high sensitivity and angular precision.

The transmitter beam pattern is measured by scanning the far-field radiated power from the chip (modulated at 1.2 MHz) in θ_x and θ_y directions. Far-field radiated power was collected by the InGaAs photodetector in the transceiver probe. The transmitter beam pattern was optimized for several points demonstrating 2D beam steering capability in both directions. The optimization corrects for the random path phase mismatches due to fabrication imperfections. Figure 5(a) demonstrates four examples of 2D beam patterns measured in four directions with clear grating lobes visible at around 9.5° spacing in both directions as expected. The cross sections of these beam patterns in θ_x and θ_y directions are shown in Figs. 5(b) and 5(c). Due to the limited scan range of our setup, we were unable to capture the full radiated power from the transmitter. The measured

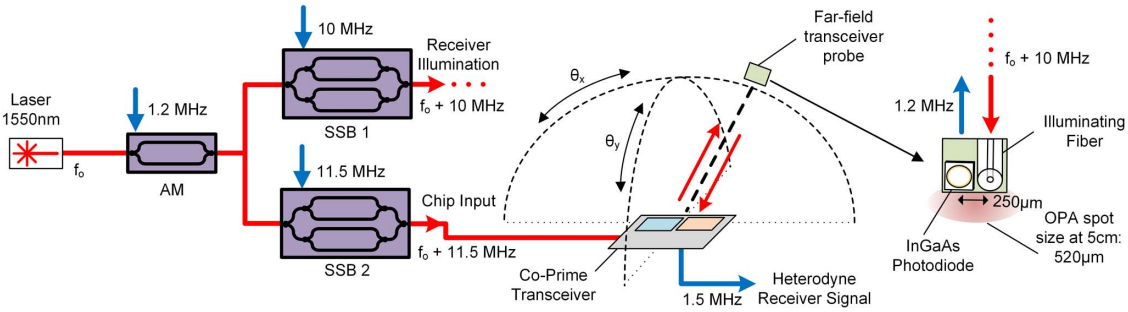

Fig. 4. Co-prime transceiver measurement setup. The far-field transceiver probe always points toward the center of rotation where the transceiver chip is located. The far-field probe consists of an InGaAs photodiode for transmitter characterization and a cleaved fiber illuminating the chip with the output of SSB 1 (input laser shifted by 10 MHz) for heterodyne receiver measurements.

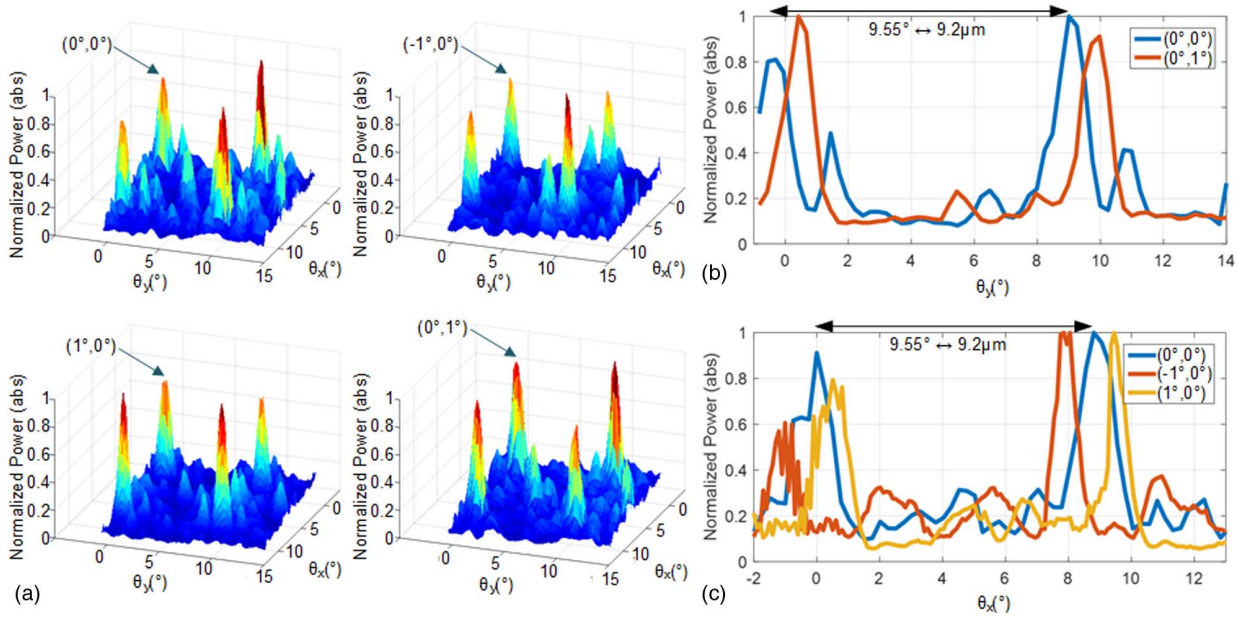

Fig. 5. Co-prime transmitter beamforming and steering using an InGaAs photodetector as the far-field probe. Grating lobes are spaced 9.55° consistent with 9.2 μm spacing of radiating elements. (a) 2D optimized beam pattern for four directions. (b) Cross section of θ_y plane. (c) Cross section of θ_x plane.

value of the SLL is affected by the non-convex search space of the transmitter beam optimization. This optimization utilizes a combination of randomized search and gradient search algorithms. The optimization changes the phase setting of the 64 phase shifters such that power in the broad-side direction is maximized. While we typically observe more than 6 dB improvement in broad-side beam power compared to the off-state of the OPA, sometimes the optimization falls short in suppressing the SLL to theoretical values. This is an artifact of the measurement apparatus and the optimization process and not a fundamental limitation of the proposed design. On-chip phase calibration schemes such as in Ref. [26] can be used to improve the SLL further.

Subsequently, the receiver array is characterized by illuminating the receiver aperture using the cleaved fiber in the transceiver probe. To remove the random phase fluctuations between the illumination and LO paths [4], the input light was externally modulated using two SSB modulators (SSB 1 and SSB 2 in Fig. 4) at 10 MHz and 11.5 MHz, respectively. The mixed downconverted signal at 1.5 MHz was amplified off-chip for processing. This setup is used to optimize the receiver beam in several directions including correcting for the random relative phase mismatches due to fabrication imperfections. Four such patterns are shown in Fig. 6(a). The grating lobes are visible at 7.2° in both directions, consistent with the design of the OPA. Cross-sectional view of these beam patterns for several directions are shown in Figs. 6(b) and 6(c). Similar to the transmitter characterization, the receiver SLL is negatively impacted by the non-convex optimization search space. In addition, heterodyne receiver measurements are more susceptible to noise. This is not a fundamental limitation of the proposed co-prime transceiver, and more complex receiver architectures such as in-phase and quadrature (IQ) receivers [27] can better suppress the undesired noise fluctuation in the received signal.

Demonstrating the 2D beam steering capability of the transmitter and the receiver array ensures that the main beam of the two apertures can be co-aligned in the same direction for all points in the 2D FOV. For a given resolvable spot (pixel), the transmitter and receiver array can be simultaneously co-aligned at that point, and the co-prime nature of the transceiver will limit in the receiver aperture to collect signal from that particular direction and suppress all signals from the grating lobes of the transmitter. To demonstrate co-prime grating-lobe suppression capability of the transceiver, the full system was characterized with concurrently active transmitter and receiver arrays. Blue patterns in Fig. 7(a) show a 1D measurement of the formed transmitter and receiver beam over a 16° range, displaying the expected grating lobes. Programming the two phased arrays simultaneously [orange patterns in Fig. 7(a)] showed that the thermal cross talk between the two patterns causes less than 0.5 dB disturbance in the main beam power of the transmitter and receiver with a worst case of 5 dB increased SLL for the transmitter array.

The combined synthesized pattern for the transceiver array is calculated by multiplication of the transmitter and receiver beam patterns, using Eq. (2), to synthesize the transceiver beam shown in Fig. 7(b). Due to the small size of our proof-of-concept transceiver, the receiver collection area is not sufficient for accurate ranging measurement compared to Refs. [28–30] with significantly larger receiver collection areas. Nonetheless, for the full scan range of 16°, the highest SLL is at −11.3 dB with a transceiver beamwidth of 0.6°, which is in close agreement with simulations and demonstrates the co-prime grating-lobe-free beamforming capability of our proposed design.

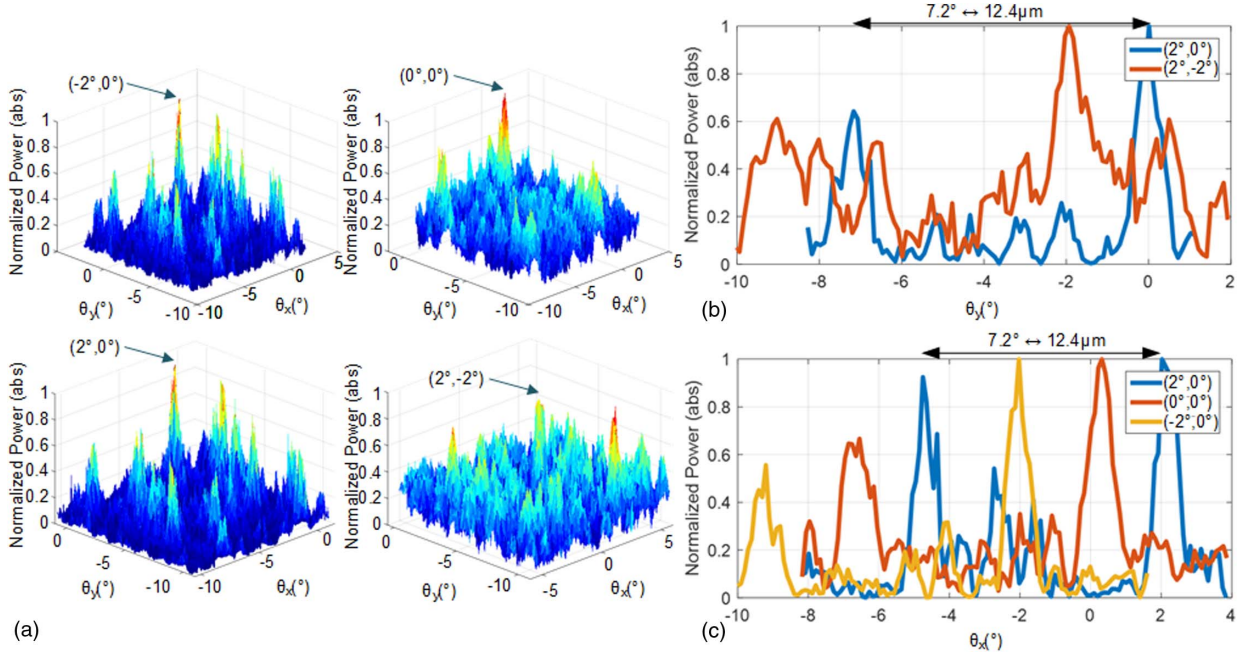

Fig. 6. Co-prime receiver beamforming and steering using a cleaved fiber for illuminating the chip with the output of SSB 1 (input laser offset by 10 MHz) and output of SSB 2 (input laser offset by 11.5 MHz) as reference signal. Grating lobes are spaced 7.2° consistent with 12.4 μm spacing of radiating elements. (a) 2D optimized beam pattern for four directions. (b) Cross section of θ_y plane. (c) Cross section of θ_x plane.

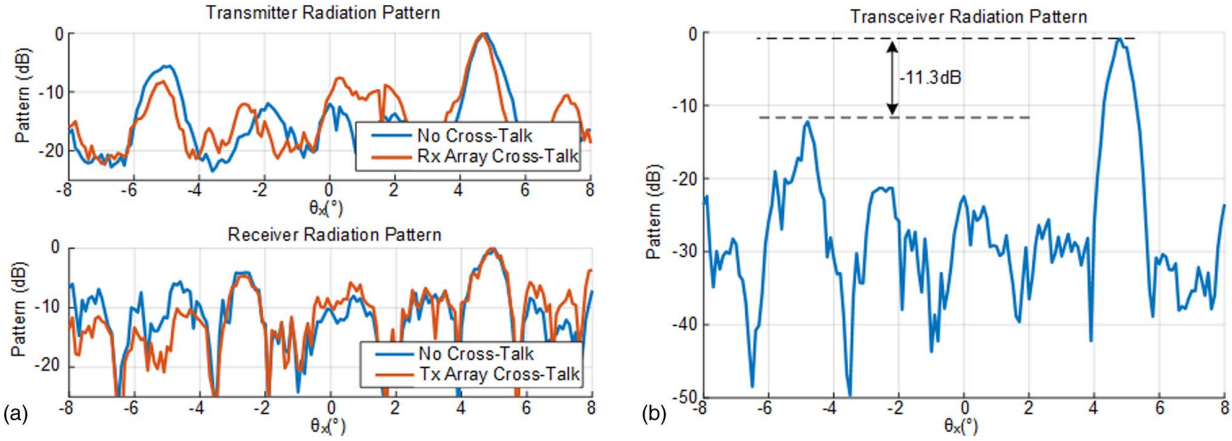

Fig. 7. Overlap plot of the transmitter and receiver patterns. (a) Beam patterns captured when the optimized settings are loaded separately (blue) and when both settings are loaded concurrently (orange). (b) Synthesized transceiver pattern.

5. DISCUSSION

The proof-of-concept implementation presented here demonstrated the realization of a co-prime transceiver architecture, achieving 1026 resolvable spots using only 128 radiating elements with only 34 electrical drivers. The advantage of this architecture is more significant for larger arrays. For example, a co-prime pair of $P = 5$ and $Q = 6$, with $d_x = 2\lambda$ and $k_1 = k_2 = 7$, will result in over 49,000 resolvable spots within the FOV of the radiator with only 2989 total radiators and phase shifter pairs requiring a total of 154 electrical drivers. This is more than an order of magnitude of reduction in the complexity of the photonics front-end and more than two orders of magnitude reduction in the number of interconnects and electrical drivers.

For a given pair of co-prime numbers, the array multiplication factors (k_1, k_2) can be increased to reduce the SLL and the beamwidth until planar routing limitations are reached for the transmitter and receiver apertures. The beamwidth can be improved beyond this limit using a larger pair of co-prime numbers.

We can also compare the effect of scaling the aperture size on the system SNR for uniform half-wavelength spacing and equivalent co-prime arrays. For uniform half-wavelength spacing apertures, increasing the transmitter and receiver aperture sizes translates to an increase in SNR. For uniform excitation of the radiators, the transmitter efficiency (defined as the ratio of the power in the 3 dB beamwidth of the main lobe and the total power radiated from the aperture) approaches 44% or −3.56 dB for large apertures, while increasing the receiver aperture size by a constant factor, N, increases the SNR by the same factor, N. In contrast, co-prime transceiver apertures experience a reduced SNR benefiting from increased aperture sizes. This is due to the fact that larger co-prime numbers result in larger transmitter inter-element spacing and an increased number of grating lobes. As a result, a larger fraction of the transmitter power is lost in the grating lobes, which reduces the transmitter gain and partially offsets the gain from the increased receiver collection area. For example, the proposed design in this paper $(P = 3, \quad Q = 4, \quad k_1 = 2, \quad k_2 = 2.67)$ with 64 receiver elements has three transmitter grating lobes within the FOV of the radiating element. For a given setting, the co-prime receiver aperture collects light from one of the three grating lobes transmitted by the transmitter aperture. Therefore, the proposed co-prime transceiver experiences an additional 4.77 dB aperture loss compared to the case with half-wavelength spacing elements with uniform excitation. The power lost in the grating lobes of the transmitter, in addition to the transmitter efficiency of a uniform array (−3.56 dB), results in the theoretical main-beam power to the input power efficiency of the proposed co-prime aperture to be −8.33 dB. After accounting for coupling inefficiencies and on-chip losses, the peak power collected by the InGaAs photodiode in the far-field transceiver probe demonstrates around 2 dB of additional loss compared to the expected theoretical value of 8.33 dB, which shows a good agreement between the analysis and the measurement result. Increasing the aperture size based on the example in this section ($P = 5$, $Q = 6$, $k_1 = k_2 = 7$) will result in 1225 receiver elements. However, the larger co-prime transmitter aperture has 12 grating lobes or 10.78 dB additional transmitter loss. It is clear that increasing the receiver area gain by a factor of 19.1 or 12.8 dB is accompanied by an increased transmitter loss of 6.01 dB, which offsets some of the SNR advantages of the larger co-prime apertures. This can be considered as the scaling limit of the co-prime transceiver.

It is worth noting that the chip area is dominated by the phase modulator, as shown in Fig. 3(d). Even if half-wavelength spacing of radiators were possible, the chip area for an equivalent half-wavelength spacing OPA would be an order of magnitude larger than that of the co-prime array. These characteristics make the co-prime transceiver architecture a very promising candidate for silicon photonics beamforming and coherent imaging applications due to the lower complexity, while achieving high resolution, low cost, and low power consumption.

Acknowledgment. The authors acknowledge Behrooz Abiri and Parham Porsandeh Khial for their valuable inputs in the design and analysis of this work.

Disclosures. The authors disclose no conflicts of interest.

Data Availability. Data underlying the results presented in this paper are not publicly available at this time but may be obtained from the authors upon reasonable request.

REFERENCES

1. M. S. Eggleston, F. Pardo, C. Bolle, B. Farah, N. Fontaine, H. Safar, M. Cappuzzo, C. Pollock, D. J. Bishop, and M. P. Earnshaw, "90 dB sensitivity in a chip-scale swept-source optical coherence tomography system," in *Conference on Lasers and Electro-Optics* (Optical Society of America, 2018), paper JTh5C.8.
2. P. P. Khial, A. D. White, and A. Hajimiri, "Nanophotonic optical gyroscope with reciprocal sensitivity enhancement," Nat. Photonics **12**, 671–675 (2018).
3. F. Aflatouni, B. Abiri, A. Rekhi, and A. Hajimiri, "Nanophotonic coherent imager," Opt. Express **23**, 5117–5125 (2015).
4. R. Fatemi, B. Abiri, and A. Hajimiri, "An 8 × 8 heterodyne lens-less OPA camera," in *Conference on Lasers and Electro-Optics* (Optical Society of America, 2017), paper JW2A.9.
5. A. White, P. Khial, F. Salehi, B. Hassibi, and A. Hajimiri, "A silicon photonics computational lensless active-flat-optics imaging system," Sci. Rep. **10**, 1689 (2020).
6. C. V. Poulton, M. J. Byrd, P. Russo, E. Timurdogan, M. Khandaker, D. Vermeulen, and M. R. Watts, "Long-range lidar and free-space data communication with high-performance optical phased arrays," IEEE J. Sel. Top. Quantum Electron. **25**, 7700108 (2019).
7. S. A. Miller, C. T. Phare, Y.-C. Chang, X. Ji, O. A. J. Gordillo, A. Mohanty, S. P. Roberts, M. C. Shin, B. Stern, M. Zadka, and M. Lipson, "512-element actively steered silicon phased array for low-power lidar," in *Conference on Lasers and Electro-Optics* (Optical Society of America, 2018), paper JTh5C.2.
8. J. Sun, E. Timurdogan, A. Yaacobi, E. S. Hosseini, and M. R. Watts, "Large-scale nanophotonic phased array," Nature **493**, 195–199 (2013).
9. A. Tuantranont, V. Bright, J. Zhang, W. Zhang, J. Neff, and Y. Lee, "Optical beam steering using MEMS-controllable microlens array," Sens. Actuators A Phys. **91**, 363–372 (2001).
10. Y. Wang, G. Zhou, X. Zhang, K. Kwon, P.-A. Blanche, N. Triesault, K. S. Yu, and M. C. Wu, "2D broadband beamsteering with large-scale MEMS optical phased array," Optica **6**, 557–562 (2019).
11. S. Chung, H. Abediasl, and H. Hashemi, "15.4 a 1024-element scalable optical phased array in 0.18 μm SOI CMOS," in *IEEE International Solid-State Circuits Conference (ISSCC)* (IEEE, 2017), pp. 262–263.
12. F. Aflatouni, B. Abiri, A. Rekhi, and A. Hajimiri, "Nanophotonic projection system," Opt. Express **23**, 21012–21022 (2015).
13. J. K. Doylend, M. J. R. Heck, J. T. Bovington, J. D. Peters, L. A. Coldren, and J. E. Bowers, "Two-dimensional free-space beam steering with an optical phased array on silicon-on-insulator," Opt. Express **19**, 21595–21604 (2011).
14. C. V. Poulton, M. J. Byrd, B. Moss, E. Timurdogan, R. Millman, and M. R. Watts, "8192-element optical phased array with 100° steering range and flip-chip CMOS," in *Conference on Lasers and Electro-Optics* (Optical Society of America, 2020), paper JTh4A.3.
15. T. Kim, P. Bhargava, C. V. Poulton, J. Notaros, A. Yaacobi, E. Timurdogan, C. Baiocco, N. Fahrenkopf, S. Kruger, T. Ngai, Y. Timalsina, M. R. Watts, and V. Stojanović, "A single-chip optical phased array in a wafer-scale silicon photonics/CMOS 3D-integration platform," IEEE J. Solid-State Circuits **54**, 3061–3074 (2019).
16. F. Ashtiani and F. Aflatouni, "$N \times N$ optical phased array with $2N$ phase shifters," Opt. Express **27**, 27183–27190 (2019).
17. N. Dostart, B. Zhang, A. Khilo, M. Brand, K. A. Qubaisi, D. Onural, D. Feldkhun, K. H. Wagner, and M. A. Popović, "Serpentine optical phased arrays for scalable integrated photonic lidar beam steering," Optica **7**, 726–733 (2020).
18. C. V. Poulton, M. J. Byrd, M. Raval, Z. Su, N. Li, E. Timurdogan, D. Coolbaugh, D. Vermeulen, and M. R. Watts, "Large-scale silicon nitride nanophotonic phased arrays at infrared and visible wavelengths," Opt. Lett. **42**, 21–24 (2017).
19. W. Ma, S. Tan, K. Wang, W. Guo, Y. Liu, L. Liao, L. Zhou, J. Zhou, X. Li, L. Liang, and W. Li, "Practical two-dimensional beam steering system using an integrated tunable laser and an optical phased array," Appl. Opt. **59**, 9985–9994 (2020).
20. R. Hansen, *Phased Array Antennas*, Wiley Series in Microwave and Optical Engineering (Wiley, 2009).
21. J. K. S. Poon and W. D. Sacher, "Multilayer silicon nitride-on-silicon photonic platforms for three-dimensional integrated photonic devices and circuits," in *75th Annual Device Research Conference (DRC)* (IEEE, 2017), pp. 1–2.
22. R. Fatemi, A. Khachaturian, and A. Hajimiri, "A nonuniform sparse 2-D large-FOV optical phased array with a low-power PWM drive," IEEE J. Solid-State Circuits **54**, 1200–1215 (2019).
23. N. Dostart, M. Brand, B. Zhang, D. Feldkhun, K. Wagner, and M. A. Popović, "Vernier Si-photonic phased array transceiver for grating lobe suppression and extended field-of-view," in *Conference on Lasers and Electro-Optics* (Optical Society of America, 2019), paper AW3K.2.
24. P. P. Vaidyanathan and P. Pal, "Sparse sensing with coprime arrays," in *Conference Record of the 44th Asilomar Conference on Signals, Systems and Computers* (IEEE, 2010), pp. 1405–1409.
25. P. P. Vaidyanathan and P. Pal, "Sparse sensing with co-prime samplers and arrays," IEEE Trans. Signal Process. **59**, 573–586 (2011).
26. J. Hulme, J. Doylend, M. Heck, J. Peters, M. Davenport, J. Bovington, L. Coldren, and J. Bowers, "Fully integrated hybrid silicon free-space beam steering source with 32-channel phased array," Proc. SPIE **8989**, 898907 (2014).
27. A. Khachaturian, R. Fatemi, and A. Hajimiri, "IQ photonic receiver for coherent imaging with a scalable aperture," arXiv:2108.10225 (2021).
28. C. V. Poulton, A. Yaacobi, D. B. Cole, M. J. Byrd, M. Raval, D. Vermeulen, and M. R. Watts, "Coherent solid-state lidar with silicon photonic optical phased arrays," Opt. Lett. **42**, 4091–4094 (2017).
29. Y. Li, B. Chen, Q. Na, Q. Xie, M. Tao, L. Zhang, Z. Zhi, Y. Li, X. Liu, X. Luo, G. Lo, F. Gao, X. Li, and J. Song, "Wide-steering-angle high-resolution optical phased array," Photon. Res. **9**, 2511–2518 (2021).
30. C. Rogers, A. Y. Piggott, D. J. Thomson, R. F. Wiser, I. E. Opris, S. A. Fortune, A. J. Compston, A. Gondarenko, F. Meng, X. Chen, G. T. Reed, and R. Nicolaescu, "A universal 3D imaging sensor on a silicon photonics platform," Nature **590**, 256–261 (2021).